AIP | The Journal of Chemical Physics

A theoretical investigation of the influence of gold nanosphere size on the decay and energy transfer rates and efficiencies of quantum emitters

Cristian A. Marocico, Xia Zhang, and A. Louise Bradley

Citation: The Journal of Chemical Physics **144**, 024108 (2016); doi: 10.1063/1.4939206
View online: http://dx.doi.org/10.1063/1.4939206
View Table of Contents: http://scitation.aip.org/content/aip/journal/jcp/144/2?ver=pdfcov
Published by the AIP Publishing

A theoretical investigation of the influence of gold nanosphere size on the decay and energy transfer rates and efficiencies of quantum emitters

Cristian A. Marocico, Xia Zhang, and A. Louise Bradley[a)]
Semiconductor Photonics Group, School of Physics and CRANN, Trinity College Dublin, College Green, Dublin 2, Ireland

(Received 7 October 2015; accepted 17 December 2015; published online 11 January 2016)

We present in this contribution a comprehensive investigation of the effect of the size of gold nanospheres on the decay and energy transfer rates of quantum systems placed close to these nanospheres. These phenomena have been investigated before, theoretically and experimentally, but no comprehensive study of the influence of the nanoparticle size on important dependences of the decay and energy transfer rates, such as the dependence on the donor-acceptor spectral overlap and the relative positions of the donor, acceptor, and nanoparticle, exists. As such, different accounts of the energy transfer mechanism have been presented in the literature. We perform an investigation of the energy transfer mechanisms between emitters and gold nanospheres and between donor-acceptor pairs in the presence of the gold nanospheres using a Green's tensor formalism, experimentally verified in our lab. We find that the energy transfer rate to small nanospheres is greatly enhanced, leading to a strong quenching of the emission of the emitter. When the nanosphere size is increased, it acts as an antenna, increasing the emission of the emitter. We also investigate the emission wavelength and intrinsic quantum yield dependence of the energy transfer to the nanosphere. As evidenced from the literature, the energy transfer process between the quantum system and the nanosphere can have a complicated distance dependence, with a r^{-6} regime, characteristic of the Förster energy transfer mechanism, but also exhibiting other distance dependences. In the case of a donor-acceptor pair of quantum systems in the presence of a gold nanosphere, when the donor couples strongly to the nanosphere, acting as an enhanced dipole; the donor-acceptor energy transfer rate then follows a Förster trend, with an increased Förster radius. The coupling of the acceptor to the nanosphere has a different distance dependence. The angular dependence of the energy transfer efficiency between donor and acceptor exhibits a strong focusing effect and the same enhanced donor-dipole character in different angular arrangements. The spectral overlap of the donor emission and acceptor absorption spectra shows that the energy transfer follows the near-field scattering efficiency, with a red-shift from the localized surface plasmon peak for small sphere sizes. © *2016 AIP Publishing LLC.* [http://dx.doi.org/10.1063/1.4939206]

I. INTRODUCTION

The optical interactions between light and matter in the presence of metal nanoparticles (NPs) is a topic of great interest, both from the point of view of a fundamental understanding of these interactions, as well as their potential applications for solar cells,[1–4] light-emitting diodes,[5–8] subwavelength imaging,[9,10] bio-sensing,[11–17] etc. Of particular importance is the influence that the *localized surface plasmon* (LSP) excited at the surface of noble metal NPs has on the optical interactions of quantum systems.[18–23]

The interaction of emitters with metallic nanospheres has been extensively studied, both theoretically[24–36] and experimentally.[37–49] There have been reports using different metallic NP size regimes and a variety of quantum dot and dye fluorophores. In Refs. 37–42, the authors studied the distance dependence of the quenching efficiency for extremely small NP, with a radius in the range 1-5 nm. The distance dependence has also been investigated for larger NP such as a Au NP with a 10 nm radius separated from a dye fluorophore[43] and a 30 nm diameter Au NP separated from a QD by 15 nm–70 nm on a triangular-shaped DNA origami platform.[44] In Ref. 45, the separation dependence is reported for a range of QD emitters in proximity to 5.5 nm Au nanospheres, whereas in Ref. 46, a selection of fluorescent molecules is attached to a Au/SiO_2 core-shell NP with a radius in the range 10-20 nm. Some studies on the specific influence of the metallic NP size on the separation dependence have also been explored. In Ref. 47, the authors report on the distance dependent quenching of Cy3 and Cy5 for two diameters of Au NP, 5 nm and 10 nm, whereas the size dependence of the quenching has been investigated for a fixed emission wavelength and quantum yield of the emitter using 3 nm, 15 nm, and 80 nm Au nanospheres in Ref. 48. Dulkeith *et al.* also reported on the influence of the Au NP size by attaching lissamine dye molecules to Au NP with radii ranging from 1 nm to 30 nm.[49] The experimental studies have revealed various distance dependences of the quenching, which include but are not limited to the r^{-6} and

a)Electronic mail: bradlel@tcd.ie

r^{-4} dependences associated with the Förster resonance energy transfer (FRET) and nano-surface energy transfer (NSET) mechanisms, respectively. The observations are influenced by the range of experimental parameters including the spectral overlap and NP size, which varied from case to case. It is noted that experiments probing the spectral dependence by varying the quantum emitter wavelength are also susceptible to changes in the quantum yield.[41,45,46]

The interaction between a quantum emitter and a metallic NP has also attracted theoretical interest, with both large and small NP considered. Anger *et al.* reported an experimental and theoretical study of the change in the radiative and non-radiative rates of a single quantum emitter as a function of its separation from an 80 nm diameter Au NP,[24] whereas Carminati *et al.* considered smaller Ag NP with a radius of 5 nm.[25] More recently, Sukharev *et al.* probed the quenching distance dependence considering Ag and Au nanospheres with radii of 20 nm and 8 nm.[26] They showed the emergence of a range of distance dependence regimes from $r^{-1.9}$ to $r^{-5.4}$. Mertens *et al.*[27] investigated the effect of the NP size for larger NP on the luminescence enhancement of the emitter, for emitters with a low quantum yield (1%) and compared the electrodynamic theory with the Gersten and Nitzan model.[28] Härtling *et al.*[35] have also studied the luminescence enhancement provided by Au nanospheres with sizes above 50 nm and its dependence on the quantum emitter position and emission wavelength.

The research to date has revealed the complexity of the quenching behavior. The quenching rate is dependent on the spectral properties and quantum yield of the quantum emitter (which are difficult to control independently experimentally) as well as its separation from the NP. Despite the large number of studies, the literature does not have a systematic and unified account of the influence of the size of the metal NP on these dependences. In this contribution, we will examine each of these dependences for a range of NP sizes. A number of features are observed including a blue shift of the spectral peak of the quenching efficiency as the Au nanosphere size increases. In addition, the r^{-6} distance dependence regime becomes smaller as the NP size increases and is no longer evident for 50 nm diameter NP.

A related, but more complex process is that of excitation energy transfer, or resonance energy transfer, in a donor-acceptor pair. This is one of the main pathways by which energy transfer occurs at the nanoscale. It plays important roles in biology,[50–53] nanophotonics (light harvesting, LEDs, nanolasers),[54–60] microscopy,[61,62] sensing,[63,64] and for optical rulers,[65] etc. The process is determined by the dipole-dipole interaction between the donor and acceptor and, in the short distance limit, has a r^{-6} dependence on the donor-acceptor separation, r, the FRET regime.[66] In free-space, this regime usually holds for donor-acceptor separations smaller than approximately 10 nm. At larger separations, the energy transfer process is overwhelmed by other de-excitation mechanisms of the donor, such as phonon relaxation or emission into the far-field. In a variety of applications, it is desirable to extend the FRET regime to larger donor-acceptor separations. This could enhance the efficiency of light harvesting and emitting devices as well as increase the range and accuracy of sensing devices and optical rulers.

Metal NP offer a way of enhancing the energy transfer rate in a donor-acceptor pair by acting as a "mediator." The role of the mediator is to increase the probability that energy transfer between donor and acceptor will occur, by providing both a large enhancement and a tight confinement of the electromagnetic field. As the energy transfer process competes with the other donor de-excitation processes, which are also possibly enhanced by the metal NP, it is the efficiency of the energy transfer process, rather than its absolute rate that is a better figure of merit for the process.

The donor-acceptor energy transfer process in the presence of metallic NP has been investigated experimentally[67–77] and theoretically[78–83] with increases in the energy transfer rate, range, and efficiency reported for various NP materials, sizes, and geometries. The experimental studies of plasmon mediated energy transfer using nanospheres have included donor-acceptor molecules in proximity to 20 nm diameter Ag nanospheres[67,68] and 40 nm Au nanospheres[69] with 21-fold and 3.2-fold increases in the FRET rate, respectively. Ref. 67 also reported an increase of approximately 57% in the characteristic energy transfer distance. A 4-fold increase in the energy transfer efficiency and ≈30% increase in the energy transfer range were observed for a core-shell geometry with separate donor and acceptor layers coating a 47 nm diameter Ag nanosphere.[70] Lunz *et al.*[71,72] tuned the energy transfer rate, efficiency, and range by varying the concentration of Au nanospheres with a diameter of 5.5 nm in a monolayer sandwiched between monolayers of donor and acceptor QDs. An increase of the FRET rate by a factor of ≈200, a ≈150 fold enhancement of the FRET efficiency, and ≈240% increase in the energy transfer distance were reported.[72] Plasmon-enhanced FRET was also observed for a similar multilayer geometry using 15 nm Au nanospheres.[73] Refs. 73 and 74 investigated the influence of preferential coupling of the metal NP to the donor or the acceptor of the FRET pair. Ref. 75 experimentally studied the impact of the metallic NP size, in the small size regime, on FRET between quantum dots. They fabricated arrays of Au nanoislands with radii up to ≈ 3.6 nm by thermal evaporation and showed that FRET between a fixed pair of quantum dots can be controlled by the metallic NP size. Theoretical studies have concentrated on one or two metallic NP sizes. Ref. 80 theoretically investigates the enhanced FRET between quantum dots in the presence of Au and Ag NP of radius equal to 4 nm. The authors of Ref. 81 also focused on small (5-10 nm) nanospheres and nanoshells, investigating non-local effects on the energy transfer process. In Ref. 82, the authors investigate the energy transfer process between chlorophyll molecules in the presence of a Au NP with a larger radius, of 25 nm. The energy transfer process has also been studied more recently in Ref. 83 for Ag spheres of 5 nm and 25 nm diameter. These are just some of the examples of studies reported in the literature. As for fluorescence quenching by metal NPs, the literature contains no systematic and unified treatment of the sphere size influence on the different dependencies of the energy transfer process between donor-acceptor pairs in the presence of a metal NP. In this

contribution, the effect of varying the metallic NP size on the distance dependence, angular position dependence, and spectral overlap dependence of the energy transfer efficiency is examined.

We begin in Sec. II by laying out briefly the theoretical framework used in our investigations. Section III A deals with the decay rate of an emitter. In Sec. III A 1, we validate the model used by comparing simulations with experimental results.[45] We next consider the decay rates of a single emitter placed near a Au NP and investigate its dependence on the emission wavelength and intrinsic quantum yield of the emitter (Sec. III A 2) and on its distance to the Au NP (Sec. III A 3), and how these dependences are influenced by the Au NP size. In Sec. III B, we consider the energy transfer rate between a donor-acceptor pair placed near the Au NP; thus, in Sec. III B 1, we validate again the model by comparing simulations with experimental results.[74] We then consider a donor-acceptor pair near a Au NP and investigate the dependence of the donor-acceptor energy transfer efficiency on the distance to the Au NP (Sec. III B 2), on the relative angular position of the donor and acceptor around the Au NP (Sec. III B 3), on the spectral overlap between donor emission, acceptor absorption and Au NP extinction spectra (Sec. III B 4) and how these dependences are influenced by the Au NP size. Finally, the conclusions are discussed in Sec. IV.

II. THEORETICAL FRAMEWORK

Using a Green's tensor formalism, which we will briefly sketch in what follows, we can calculate the energy transfer rate and efficiency between two point dipoles placed near a metal NP. This formalism, described in more detail elsewhere,[84–86] is particularly suited to our present investigation, since it uses the full electrodynamic response of the Au NP, without making approximations that would not be valid over the entire range of Au NP sizes we consider, as simpler models do (Gersten-Nitzan,[28] FRET[66]).

A. Decay rates

Considering a two-state quantum system modeled as an electric point dipole, its decay rate in the presence of the Au NP can be related to the power emitted as[87]

$$\frac{\gamma(\mathbf{r},\omega)}{\gamma_0(\omega)} = \frac{P(\mathbf{r},\omega)}{P_0(\omega)}, \tag{1}$$

where $\gamma(\mathbf{r},\omega)$ and $\gamma_0(\omega)$ are the decay rates of the quantum system in the presence and absence of the Au NP, respectively, and $P(\mathbf{r},\omega)$ and $P_0(\omega)$ are the power emitted by the dipole in the presence and absence of the Au NP, respectively.

The emitted power in the absence of the Au NP, $P_0(\omega)$ has the classical expression[87]

$$P_0(\omega) = \frac{\sqrt{\epsilon}\omega^4\mu_0^2}{12\pi\varepsilon_0 c^3}, \tag{2}$$

where $\sqrt{\epsilon}$ is the refractive index of the host medium, ω is the emission frequency, and μ_0 is the transition dipole moment of the emitter. The emitted power can be calculated from the integral of the normal component of the Poynting vector along a closed surface containing the quantum system,

$$P(\mathbf{r}_0,\omega) = \frac{1}{2}\mathrm{Re}\oint \mathrm{d}\Omega\, \hat{\mathbf{n}}\cdot\mathbf{E}(\mathbf{r},\omega)\times\mathbf{H}^*(\mathbf{r},\omega), \tag{3}$$

where now $\hat{\mathbf{n}}$ is the unit vector normal to the surface, and $\mathbf{E}$ and $\mathbf{H}$ are the electric and magnetic fields, respectively. The total and radiated emitted power can be calculated from this expression by letting the imaginary surface shrink to a point or be infinite. The total power emitted in the presence of the sphere is

$$\begin{aligned} P(\mathbf{r}_0,\omega) &= \frac{1}{2}\,\mathrm{Re}\oint \mathrm{d}\Omega\, \hat{\mathbf{n}}\cdot\mathbf{E}(\mathbf{r},\omega)\times\mathbf{H}^*(\mathbf{r},\omega)\Big|_{\mathbf{r}\to\mathbf{r}_0} \\ &= \left|\frac{\mathbf{E}_2(\mathbf{r}_0,\omega)}{\mathbf{E}_0(\mathbf{r}_0,\omega)}\right|^2\left[1+\frac{6\pi c}{\sqrt{\epsilon}\omega}\mathrm{Im}\left(\hat{\mathbf{n}}\cdot\mathfrak{G}(\mathbf{r}_0,\mathbf{r}_0,\omega)\cdot\hat{\mathbf{n}}\right)\right], \end{aligned} \tag{4}$$

where $\mathfrak{G}(\mathbf{r}_0,\mathbf{r}_0,\omega)$ is the Green's tensor, and the prefactor in the second line is the field enhancement factor, $A(\mathbf{r}_0,\omega) = |\mathbf{E}_2(\mathbf{r}_0,\omega)/\mathbf{E}_0(\mathbf{r}_0,\omega)|^2$. Similarly, the radiative power emitted in the presence of the sphere is

$$P_\mathrm{r}(\mathbf{r}_0,\omega) = \frac{1}{2}\mathrm{Re}\oint \mathrm{d}\Omega\, \hat{\mathbf{n}}\cdot\mathbf{E}(\mathbf{r},\omega)\times\mathbf{H}^*(\mathbf{r},\omega)\Big|_{r\to\infty}. \tag{5}$$

These general expressions take, for a spherical NP, specific forms depending on the orientation of the transition dipole of the quantum system with respect to the NP. For a radially oriented transition dipole, the radiated and total emitted power become

$$\frac{P_\mathrm{r}^\perp(\mathbf{r}_0,\omega)}{P_0(\omega)} = A(\mathbf{r}_0,\omega)\frac{3}{2}\sum_m m(m+1)(2m+1)\left|\frac{\psi_m(\rho_\mathrm{s})+a_m\zeta_m(\rho_\mathrm{s})}{\rho_\mathrm{s}^2}\right|^2, \tag{6a}$$

$$\frac{P^\perp(\mathbf{r}_0,\omega)}{P_0(\omega)} = A(\mathbf{r}_0,\omega)\left[1+\frac{3}{2}\sum_m m(m+1)(2m+1)\mathrm{Re}\left(\frac{a_m\zeta_m^2(\rho_\mathrm{s})}{\rho_\mathrm{s}^4}\right)\right], \tag{6b}$$

$$\frac{P_\mathrm{nr}^\perp(\mathbf{r}_0,\omega)}{P_0(\omega)} = \frac{P^\perp(\mathbf{r}_0,\omega)}{P_0(\omega)} - \frac{P_\mathrm{r}^\perp(\mathbf{r}_0,\omega)}{P_0(\omega)}, \tag{6c}$$

while the same quantities for a tangentially oriented dipole read

$$\frac{P_{\mathrm{r}}^{\parallel}(\mathbf{r}_0,\omega)}{P_0(\omega)} = A(\mathbf{r}_0,\omega)\frac{3}{4}\sum_m (2m+1)\left[\left|\frac{\psi_m(\rho_{\mathrm{s}})+b_m\zeta_m(\rho_{\mathrm{s}})}{\rho_{\mathrm{s}}}\right|^2 + \left|\frac{\psi'_m(\rho_{\mathrm{s}})+a_m\zeta'_m(\rho_{\mathrm{s}})}{\rho_{\mathrm{s}}}\right|^2\right], \tag{7a}$$

$$\frac{P^{\parallel}(\mathbf{r}_0,\omega)}{P_0(\omega)} = A(\mathbf{r}_0,\omega)\left[1+\frac{3}{4}\sum_m (2m+1)\mathrm{Re}\left(\frac{b_m\zeta_m^2(\rho_{\mathrm{s}})}{\rho_{\mathrm{s}}^2}+\frac{a_m\zeta_m'^2(\rho_{\mathrm{s}})}{\rho_{\mathrm{s}}^2}\right)\right], \tag{7b}$$

$$\frac{P_{\mathrm{nr}}^{\parallel}(\mathbf{r}_0,\omega)}{P_0(\omega)} = \frac{P^{\parallel}(\mathbf{r}_0,\omega)}{P_0(\omega)} - \frac{P_{\mathrm{r}}^{\parallel}(\mathbf{r}_0,\omega)}{P_0(\omega)}. \tag{7c}$$

In all the above expressions, the summation is over the multipole moments m of the sphere, ψ_m and ζ_m represent the first and third kind Riccati-Bessel functions, $\rho_{\mathrm{s}} = kr_0$, and a_m and b_m are the Mie scattering coefficients of the sphere. The relative decay rates can now be calculated from Eq. (1).

B. Energy transfer rate

The energy transfer (ET) rate between donor and acceptor quantum systems can be calculated similar to the decay rates from the expression

$$\frac{\gamma_{\mathrm{DA}}(\mathbf{r}_{\mathrm{A}},\mathbf{r}_{\mathrm{D}},\omega)}{\gamma_0(\omega)} = \frac{P_{\mathrm{DA}}(\omega)}{P_0(\omega)}, \tag{8}$$

where $P_{\mathrm{DA}}(\omega)$ represents the power emitted by the donor D and absorbed by the acceptor A.

It can be shown that the ET rate between a donor-acceptor pair modeled as point dipoles is given as[74]

$$\begin{aligned}\gamma_{\mathrm{DA}}(\mathbf{r}_{\mathrm{A}},\mathbf{r}_{\mathrm{D}}) &= \int_0^\infty \mathrm{d}\omega f_{\mathrm{D}}(\omega)\gamma_{\mathrm{DA}}(\mathbf{r}_{\mathrm{A}},\mathbf{r}_{\mathrm{D}},\omega)\\ &= 18\pi\frac{Y_D}{\tau_{\mathrm{D}}}\int_0^\infty \mathrm{d}\omega f_{\mathrm{D}}(\omega)|\mathbf{n}_{\mathrm{A}}\cdot\mathfrak{G}(\mathbf{r}_{\mathrm{A}},\mathbf{r}_{\mathrm{D}},\omega)\cdot\mathbf{n}_{\mathrm{D}}|^2\sigma_{\mathrm{A}}(\omega),\end{aligned} \tag{9}$$

where τ_{D} is the donor lifetime in the absence of the acceptor, Y_{D} is the quantum yield of the donor, and $f_{\mathrm{D}}(\omega)$ is the area-normalized donor emission spectrum, i.e., $\int_0^\infty \mathrm{d}\omega f_{\mathrm{D}}(\omega) = 1$, $\sigma_{\mathrm{A}}(\omega)$ is the acceptor absorption cross section and $\mathfrak{G}(\mathbf{r}_{\mathrm{A}},\mathbf{r}_{\mathrm{B}},\omega)$ is the Green's tensor in the particular geometry. Finally, $\mathbf{n}_{\mathrm{D(A)}}$ is a unit vector along the direction of the transition dipole moment of the donor (acceptor).

The area-normalized emission spectrum is also used to account for real emitters in the decay rates. In the case of the experimental verification, Secs. III A 1 and III B 1, the emission spectrum is taken from experiments, whereas for our purely theoretical calculations, we use a Gaussian function with a FWHM of approximately 45 nm for the emission spectrum.

III. RESULTS AND DISCUSSION

A. Decay rates

As previously described, the decay rates of quantum emitters near metallic NP have been studied both theoretically[24–34,36] and experimentally[37–49] for a variety of NP sizes. However, a systematic investigation of the influence of the metal NP size on the several dependencies of the decay rates has not been undertaken and that is what we investigate in this section.

1. Experimental verification

Before presenting the theoretical study, we first validate our model by direct comparison with experimental data previously reported in Ref. 45. Fig. 1(a) shows a schematic of the experimental samples, prepared using a Layer-by-Layer technique.[88] A monolayer of Au nanospheres with a radius $a = 2.75$ nm is separated by a polyelectrolyte layer of thickness d (not shown here) from a monolayer of closely packed quantum dots (blue spheres). Fig. 1(b) presents the optical properties of the quantum dots and the Au NP. The black and red curves represent the emission spectra of two sizes of CdTe quantum dots, labeled QD-1 and QD-3 in Ref. 45 and in the rest of this paper, whereas the blue curve represents the extinction spectrum of the Au NP monolayer. The photoluminescence (PL) spectra and the time-resolved PL decays of these samples were recorded. The quenching of the QD emission was calculated from these data sets. The PL quenching was calculated as $Q_{\mathrm{PL}} = 1 - I_{\mathrm{onAu}}/I_{\mathrm{QD}}$, where I_{onAu} (I_{QD}) represents the integrated spectral emission of the QD monolayer in the presence (absence) of the Au NP monolayer. Similarly, the lifetime quenching was calculated as $Q_{\mathrm{LT}} = 1 - \tau_{\mathrm{onAu}}/\tau_{\mathrm{QD}}$, with τ_{onAu} (τ_{QD}) being the PL decay times of the QD monolayer in the presence (absence) of the Au NP monolayer. Figs. 1(c) and 1(d) show the PL and lifetime quenching efficiencies as red squares and blue diamonds, respectively, for the two sizes of quantum dots. The agreement between the PL and lifetime quenching for each one of the two panels, within the error bars, shows that the radiative decay rate of the quantum dots is not modified significantly by the presence of the Au NP monolayer. We also show two theoretical fits of the experimental data with the FRET model (red dashed curve) and the NSET model (blue dotted curve).

The results of our simulation, using the Green's tensor formalism, are shown as a continuous black line in Figs. 1(c) and 1(d). The simulations have been performed using the experimental values of the QD properties — size, quantum yield, emission spectrum — and Au NP properties — size and concentration in the monolayer. The expressions for the emitted power, Eqs. (6) and (7), are now extended to account

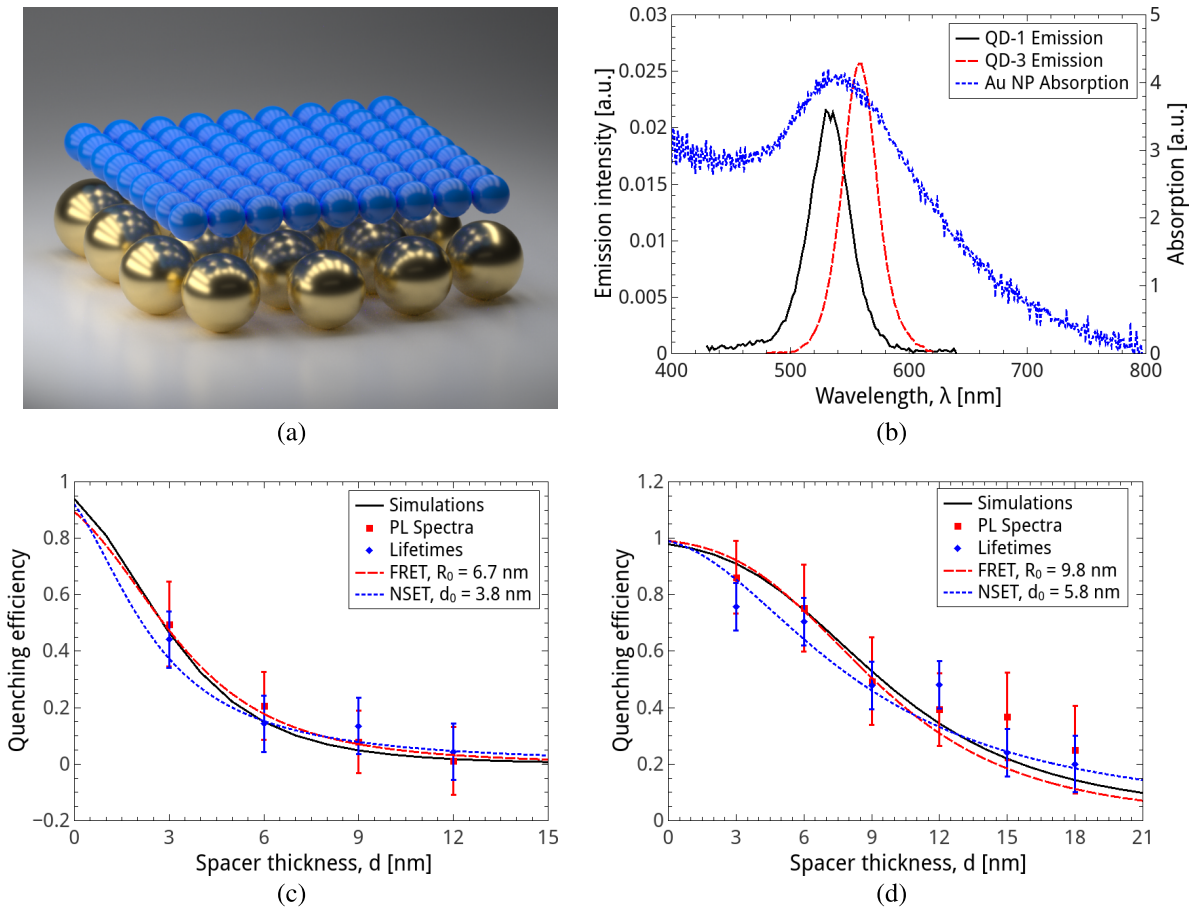

FIG. 1. Experimental verification of the model used in this paper; (a) schematic of the QD monolayer (blue spheres) on top of the Au NP monolayer (gold spheres); (b) normalized emission spectra of the two quantum dot samples, as well as the extinction spectrum of the Au NP. The experimental data sets are taken from Ref. 45 for the quantum dots labeled as (c) QD-1 and (d) QD-3 in that reference. The black curve shows our parameter-free simulation. The red dashed curve is a fit of the experimental data with a FRET model, while the blue dotted curve corresponds to a fit of the experimental data with a NSET model.

for the multiple Au NPs in the monolayer by employing a multiple scattering technique, as discussed in Ref. 89. Using the experimental concentration of Au NPs in the monolayer, an average is performed over a large number of realizations of the Au NP distribution in the monolayer. Theoretically, quenching of the emission is due to energy transfer from the emitter to the Au NP and absorption in the latter. The theoretical non-radiative decay efficiency can be calculated as

$$Q_{\text{th}} = \frac{\gamma_{\text{NP}}}{\gamma_{\text{r}} + \gamma_{\text{nr}}^{0} + \gamma_{\text{NP}}}, \tag{10}$$

where γ_{r} is the radiative decay rate, γ_{nr}^{0} is the intrinsic non-radiative decay rate of the quantum dots, when the quantum yield is less than 100%, and γ_{NP} is the non-radiative decay rate of the emitter due to absorption in the Au NP. The simulation uses no free parameters. It can be noted that, while both theoretical fits and our simulations agree with the experimental data within the error bars, the characteristic distances extracted from the FRET fit do not agree with those calculated from the spectral overlap (see Ref. 45 for a more in-depth discussion). There are many experiments suggesting that the ET mechanism from the quantum dot to the Au NP has a more complex distance dependence than the FRET and NSET models allow for. We will investigate this distance dependence and how it is affected by the Au NP size in more detail in Section III A 3.

2. *Emission wavelength and quantum yield dependence of the decay rates*

Now that the theoretical model and simulation procedure have been validated experimentally, we consider the simple case of a single emitter placed close to a single Au NP. We investigate the influence of the Au NP size on the dependence of the non-radiative decay efficiency of the emitter on its emission wavelength and intrinsic quantum yield. The emission spectrum of the quantum emitter will be modeled as a Gaussian distribution with a varying central wavelength and a full-width at half-maximum (FWHM) of ≈45 nm, typical of fluorophores such as dyes. We also introduce a slightly different non-radiative decay efficiency as

$$\eta' = 10 \log_{10} \frac{\eta}{1-\eta}, \quad \text{with} \quad \eta = Q_{\text{th}} = \frac{\gamma_{\text{NP}}}{\gamma_{\text{r}} + \gamma_{\text{nr}}^{0} + \gamma_{\text{NP}}}; \tag{11}$$

thus, a $\eta = 50\%$ non-radiative decay efficiency corresponds on this scale to $\eta' = 0$.

Fig. 2(a), for which the intrinsic quantum yield of the emitter is $Y_0 = 100\%$ shows the non-radiative decay efficiency, η', as a function of the emission wavelength of

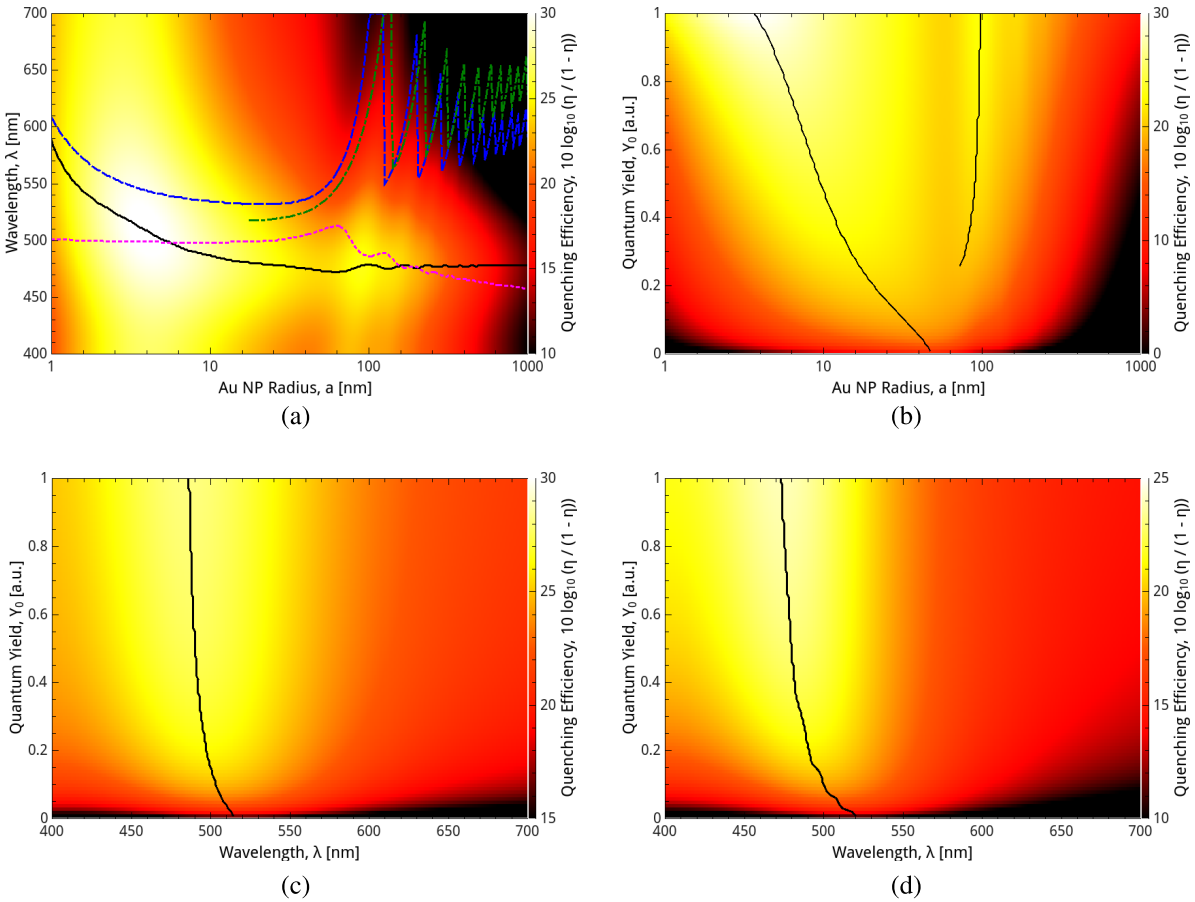

FIG. 2. (a) Emission wavelength and Au NP size dependence of the non-radiative decay efficiency, η', for an emitter with an intrinsic quantum yield of $Y_0 = 100\%$; the solid black line represents the wavelength of the maximum non-radiative decay efficiency, the dotted magenta, dash-dotted green, and dashed blue lines represent the wavelength of maximum absorption, far-field scattering, and near-field scattering efficiencies, respectively. (b) Quantum yield and Au NP size dependence of the non-radiative decay efficiency for an emission wavelength $\lambda_{em} = 525$ nm; the black lines are guides for the eye representing the maxima in the non-radiative decay efficiency. Quantum yield and emission wavelength dependence of the non-radiative decaying efficiency for a Au NP with radius (c) $a = 10$ nm and (d) $a = 50$ nm; the black lines are guides for the eye.

the quantum emitter, λ_{em}, and the radius of the Au NP, a. The radius of the Au NP varies from 1 nm to 1 μm, on a logarithmic scale, and the emitter is placed at a distance $d = 3$ nm from the surface of the Au NP. Superimposed on the contour plot, there are several curves which we will now discuss. The solid black line represents the wavelength of the maximum non-radiative decay efficiency, η', for each value of the Au NP radius, a. There is an evident blue-shift from $\lambda_{max} \approx 580$ nm to $\lambda_{max} \approx 500$ nm in the wavelength of the maximum non-radiative decay efficiency as the Au NP radius is increased from $a = 1$ nm to $a \approx 10$ nm. For larger radii, the blue-shift continues slightly, after which the wavelength hardly changes with radius. The other three lines in the panel represent wavelengths of the maximum absorption (dotted magenta), scattering (dash-dotted green), and near-field scattering (dashed blue) efficiencies. The scattering efficiency is only relevant when the size of the Au NP is sufficiently large, whereas absorption dominates for sizes smaller than $a = 50$ nm. However, for these small sizes, the wavelength of maximum absorption remains roughly constant at $\lambda_{max} = 500$ nm and does not undergo the same blue-shift as the wavelength of maximum non-radiative decay efficiency, with increasing Au NP size. Thus, neither the scattering or absorption efficiencies explain the blue-shift for small Au NP sizes, although they do describe the oscillations of the wavelength of maximum non-radiative decay efficiency for sizes larger than $a \approx 100$ nm. The near-field scattering efficiency, on the other hand, does a much better job for small Au NP sizes. This quantity is the near-field analog of the far-field scattering efficiency, obtained by calculating the power radiated out of a sphere of finite (usually small) radius, in this case $r = a + d = a + 3$ nm. This efficiency is, therefore, sensitive to the same near-field that the emitter experiences, and the non-radiative decay efficiency of the emitter follows rather closely the near-field scattering efficiency for small Au NP sizes. For larger sizes, the trends of the near- and far-field scattering are essentially the same, consisting of red-shifts of particular peaks which are associated with higher order multipoles of the sphere, followed by the apparition of new peaks at low wavelengths.

Fig. 2(b) shows the non-radiative decay efficiency of the emitter as a function of Au NP radius and quantum yield, considering an emission wavelength of $\lambda_{em} = 525$ nm. The general trend is that, as the quantum yield increases, so does the non-radiative decay efficiency for the emitter. The explanation for this is that the intrinsic non-radiative rate of the emitter, i.e., the decay rate through other relaxation processes, increases with decreasing quantum yield, thus also increasing

the total decay rate of the emitter and, hence, lowering the non-radiative decay efficiency. In addition to this general increase in the non-radiative decay efficiency with quantum yield, the panel shows a number of peaks in the non-radiative decay efficiency as a function of Au NP size: there is a main peak for small sizes, below $a = 50$ nm, and a number of less pronounced peaks when $a > 100$ nm. Considering the main peak, it undergoes a shift from $a = 50$ nm at low quantum yields, $Y_0 \approx 1\%$, to $a \lessapprox 10$ nm at the highest quantum yields, $Y_0 = 100\%$. The shift is traced in the panel by the black line, which acts as guide to the eye. Again, with decreasing quantum yield, the non-radiative decay efficiency will decrease as well. In these circumstances, a larger Au NP size has, in this regime, a stronger non-radiative interaction with the emitter, thus compensating the larger intrinsic non-radiative decay rate of the emitter. For the secondary peaks, however, the shift is in the opposite direction, though much less pronounced, since for the larger Au NP, the radiative interaction with the emitter dominates over the non-radiative interaction.

Finally, Figs. 2(c) and 2(d) show the joint emission wavelength and quantum yield dependence of the non-radiative decay efficiency for two Au NP sizes, $a = 10$ nm and $a = 50$ nm. The first thing to notice is that the general form of the emission wavelength/quantum yield dependence is similar for the two Au NP sizes. There is a peak around $\lambda_{em} = 500$ nm, corresponding to the LSP of the Au NP, which undergoes a slight blue-shift as the quantum yield is increased. There are a number of additional points to be made regarding the joint dependence of the non-radiative decay efficiency on the emission wavelength and the intrinsic quantum yield of the emitter. Whereas the non-radiative decay efficiency increases monotonically with the intrinsic quantum yield of the emitter, as expected, its dependence on the emission wavelength exhibits a maximum in the vicinity of the LSP peak. It is therefore important that in experiments investigating the emission wavelength dependence of the non-radiative decaying efficiency of a quantum emitter, one ascertains whether the intrinsic quantum yield of the quantum emitter also changes, as changes in this variable may determine the wavelength of the maximum non-radiative decay efficiency that one observes.

3. Distance dependence of the decay rates

To investigate the influence of the Au NP size on the dependence of the non-radiative decay efficiency on the distance between the quantum emitter and the center of the Au NP, r, we consider that we can write the rate of ET from the emitter to the Au NP as

$$\frac{\gamma_{NP}(\mathbf{r})}{\gamma_0} = \left(\frac{R_0}{r}\right)^n, \tag{12}$$

where R_0 is the so-called characteristic distance at which the non-radiative decay efficiency is 50% and n is an exponent, which, as mentioned in the Introduction, takes the value $n = 6$ for the FRET model and the value $n = 4$ for the NSET model. With this expression for the ET rate, the logarithmic form of the non-radiative decay efficiency becomes

$$\eta' = 10\, n \log_{10} R_0 - 10\, n \log_{10} r, \tag{13}$$

which leads to

$$n(r) = -\frac{1}{10}\frac{d\eta'}{d(\log_{10} r)}. \tag{14}$$

The emission wavelength of the quantum emitter has been fixed at $\lambda_{em} = 525$ nm, with an intrinsic quantum yield of $Y_0 = 100\%$. The value of the quantum yield of the emitter does not affect the exponent n, only the overall values of the ET rate.

Fig. 3(a) shows a contour plot of the exponent n of the distance dependence of the rate of ET from the quantum emitter to the Au NP as a function of the distance between the emitter and the surface of the Au NP, $d = r - a$, and Au NP size, from $a = 1$ nm to $a = 1$ μm. The panel shows that, close to the surface of the Au NP, $d \lessapprox a/4$, the non-radiative decay efficiency increases dramatically with decreasing d, having large values of the exponent n. This is due to the strong coupling of the emitter to the high order multipoles of the Au sphere, which have a very limited spatial range. When the distance between the emitter and the surface of the Au NP becomes larger than $d \approx a/4$, and the Au NP radius is reasonably small, $a \lessapprox 100$ nm, the exponent becomes $n \approx 6$, characteristic of the FRET regime. For these values of the parameters, the emitter-Au NP interaction is essentially

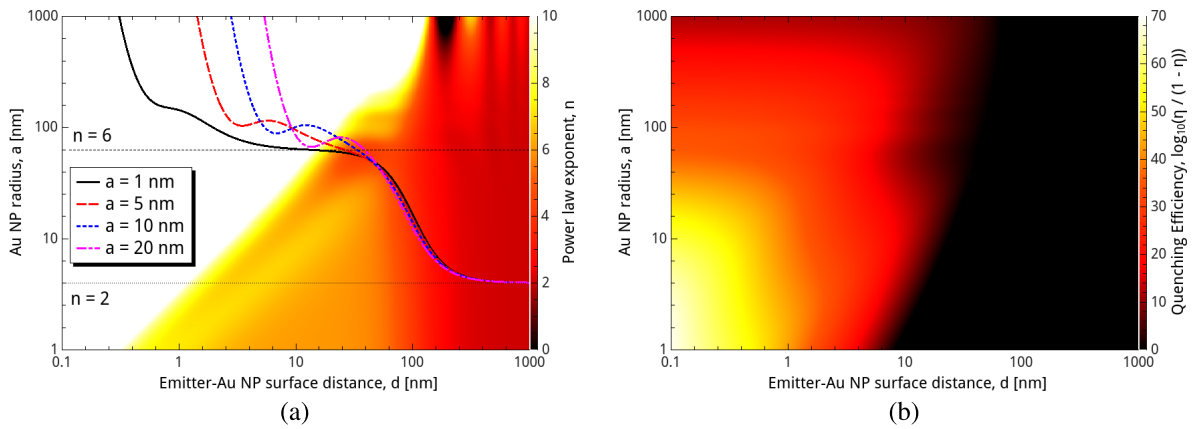

FIG. 3. (a) Exponent n of the non-radiative decay efficiency of the quantum emitter near the Au NP as a function of the emitter distance to the surface of the Au NP, d, and the Au NP size, a; the individual curves represent the exponent n as a function of d for several values of the Au NP size, a. (b) The non-radiative decay efficiency as a function of Au NP size, a, and emitter distance to the surface of the Au NP, d. The emission wavelength of the quantum emitter is $\lambda_{em} = 525$ nm and its intrinsic quantum yield is $Y_0 = 100\%$.

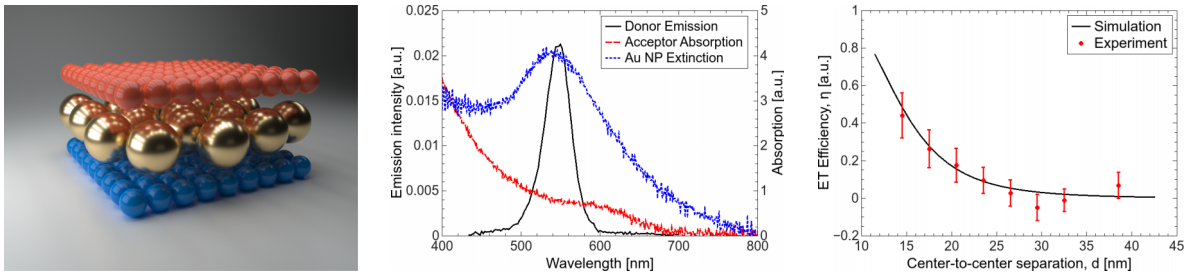

(a) (b) (c)

FIG. 4. (a) Schematic of the Au nanosphere monolayer (radius 2.75 nm) sandwiched between a donor QD monolayer (blue spheres) and an acceptor QD monolayer (red spheres). (b) Emission spectrum of donor QD monolayer (black solid line), absorption spectrum of the acceptor QD monolayer (red dashed line), and extinction of Au NP monolayer (blue dotted line). (c) Energy transfer efficiency *versus* the center-to-center distance for monolayers of quantum dots separated by a monolayer of Au nanospheres of radius 2.75 nm. The donor-Au NP separation is kept fixed at 3 nm. See Ref. 74. The black solid line represents our simulation results.

dipole-dipole. Finally, when $d \gtrapprox 100$ nm, the emitter-Au NP interaction becomes radiative with a characteristic r^{-2} distance dependence. Notice that the onset of the radiative regime does not depend on the size of the Au NP, as did the FRET regime, but it occurs always at $d \approx 100$ nm, regardless of size. The curves superimposed on the contour plot in Fig. 3(a) represent the exponent n as a function of d for several Au NP sizes. The dependence of the onset of the FRET regime on Au NP is clearly visible, as is the independence of the onset of the radiative regime.

Fig. 3(b) shows the actual values of the non-radiative decay efficiency from which the exponent n was extracted over the same range of Au NP sizes, a, and emitter distance to the Au NP surface as in Fig. 3(a). It is clear that, up to distances of a few nanometers, non-radiative decay dominates the decay process of the emitter, as evidenced by the positive values of the non-radiative decay efficiency η' over that range. For larger distances, η' also takes negative values, though they have been suppressed in the figure for visibility. The strongest non-radiative decay takes place very close to the smallest Au NP, since these contribute almost nothing to increase the radiative decay rate of the emitter.

B. Energy transfer rates

There have been numerous experimental[67–77] and theoretical[78–83] studies of the ET process in donor-acceptor pairs. The studies reported increases in the ET rate, range, and efficiency for various NP materials, sizes, and geometries. As in the case of fluorescence quenching by metal NPs, the literature contains no systematic and unified treatment of the sphere size influence on the different dependences of the ET process between donor-acceptor pairs in the presence of a metal NP. In this section, we consider the effect of the metallic NP size on the distance dependence, angular dependence, and spectral overlap dependence of the ET efficiency.

1. Experimental verification

As before, we validated the model by comparing it with experimental measurements of ET rates between monolayers of donor and acceptor QDs, separated by a monolayer of Au nanospheres.[74] The schematic of the structure is presented in Fig. 4(a), where the donor QDs are represented as blue spheres in the bottom monolayer, the acceptor quantum dots are represented as red spheres in the top monolayer, and the Au NP are represented as gold spheres in the middle monolayer. As before, the separation of the different monolayers is controlled by the use of polyelectrolyte layers of known thickness (not shown in the schematic). Fig. 4(b) shows the emission spectrum of the donor QD monolayer (black continuous line), the absorption spectrum of the acceptor QD monolayer (red dashed line), and the extinction spectrum of the Au NP monolayer, showing the LSP peak (blue dotted line). This panel shows a good overlap between the different spectra, an essential feature for optimizing the ET process. Finally, Fig. 4(c) shows the calculated ET efficiency as a function of the center-to-center separation between the donor and acceptor quantum dot monolayers, together with the experimental measurements. In this multilayer structure, the donor-Au NP separation is kept fixed at 3 nm, and the acceptor-Au NP separation is varied. Again, the simulation uses experimental values of all parameters and is, therefore, parameter-free. As in the case of the decay rates, the presence of multiple Au NPs in the monolayer is taken into account via a multiple scattering technique[89] and an average is performed over a large number of realizations of the Au NP distribution in the monolayer. Furthermore, the total ET rate is a sum of ET rates from the donor to individual acceptors tightly packed in the acceptor monolayer.[90] The experimental results are shown as red discs, while the results of the simulations are presented as the black solid line. A good agreement between the model and experiment is observed. Having validated the model via comparison with experiments, we will now use this model in the following investigation of the influence of the Au NP size on the distance, angular position, and spectral overlap dependencies of the ET efficiency.

2. Distance dependence of the energy transfer

We consider a single donor-Au NP-acceptor triad. In this, as well as Subsections III B 3 and III B 4, the intrinsic quantum yield of the donor is $Y_0^D = 100\%$, and the donor emission spectrum is modeled as a Gaussian with a FWHM ≈45 nm, with a similar shaped absorption spectrum for the acceptor. The peak wavelengths of the donor emission and

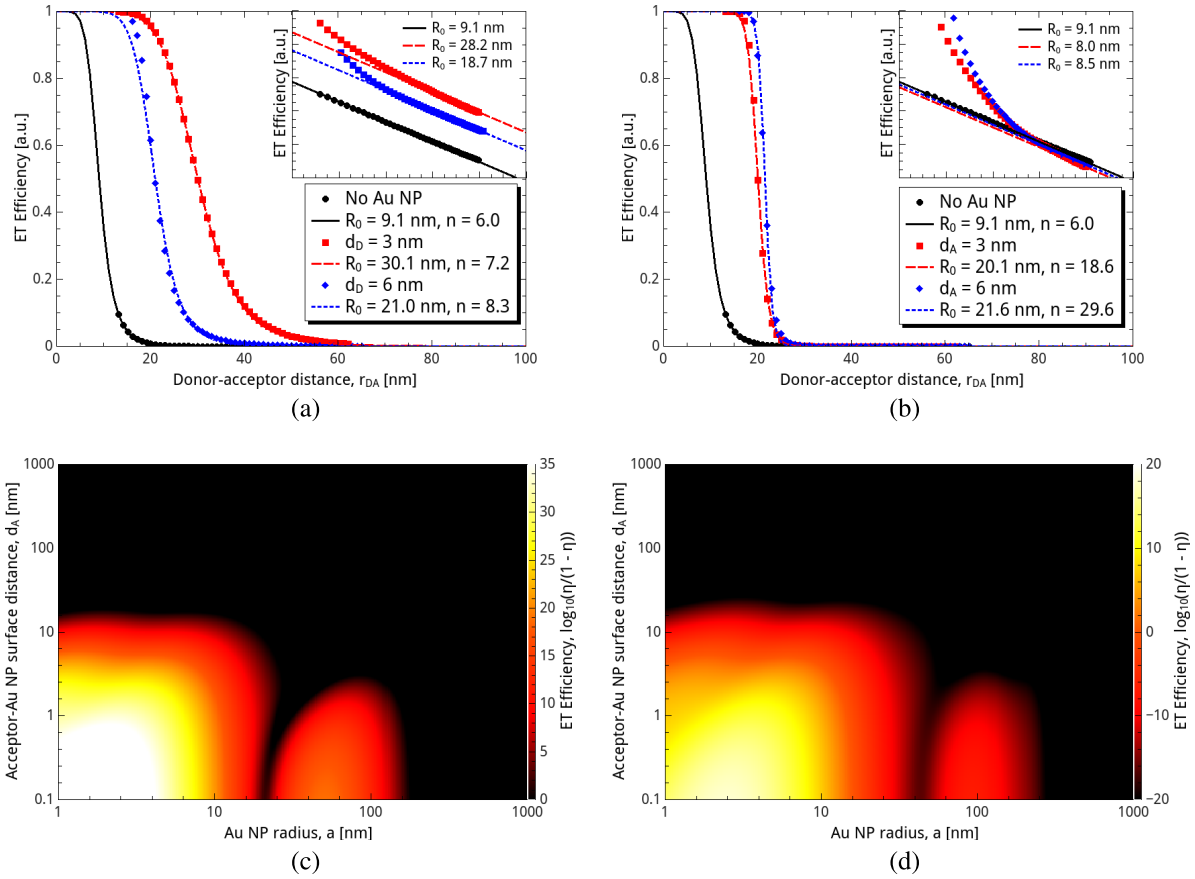

FIG. 5. Energy transfer efficiency η between a donor-acceptor pair on opposite sides of the Au NP for (a) fixed Au NP size, $a = 5$ nm, fixed donor positions, varying positions of the acceptor; (b) fixed Au NP size, $a = 5$ nm, fixed acceptor positions, varying positions of the donor. The solid black line in each panel represents the ET efficiency in the absence of the Au NP. The ET efficiency η' as a function of Au NP size and acceptor position for fixed positions of the donor at (c) $d_D = 3$ nm and (d) $d_D = 6$ nm from the surface of the Au NP. The donor emission and acceptor absorption peak wavelengths are $\lambda_{em} = \lambda_{abs} = 525$ nm.

acceptor absorption spectra will be specified for each case considered.

We first investigate how the size of the Au NP influences the dependence of the ET efficiency between a donor-acceptor dipole pair, on their separation. The donor and acceptor are placed on opposite sides of the Au NP, forming a linear triad. Fig. 5 shows the distance dependence of the ET efficiency from donor to acceptor. Fig. 5(a) considers a Au NP of radius $a = 5$ nm and a donor whose distance to the surface of the Au NP is constant and equal to $d_D = 3$ nm and $d_D = 6$ nm, respectively. The acceptor distance to the surface of the Au NP, d_A, is varied, and we plot the ET efficiency as a function of the total donor-acceptor distance $r_{DA} = d_D + 2a + d_A$. The black circles correspond to a donor-acceptor pair in free-space, while the solid black line represents a fit with a power law model of the form $(R_0/r_{DA})^n$, with R_0 and n being the fitting parameters. The legend gives the extracted values of these parameters as $R_0 = 9.1$ nm and $n = 6$, which corresponds to a FRET model with a characteristic distance of 9.1 nm. The characteristic distance, also known as the Förster radius in the FRET model, is the donor-acceptor distance at which the ET efficiency is $\eta = 50\%$. The second set of red squares corresponds to a donor placed at $d_D = 3$ nm from the surface of the Au NP. The red dashed line represents a fit with the same functional form, and it yields the following values for the fitting parameters: $R_0 = 30.1$ nm and $n = 7.2$. The fit is performed in the range where $\eta \approx 50\%$ and it shows a considerable increase of the characteristic distance from $R_0 = 9.1$ nm to $R_0 = 30.1$ nm. The exponent $n = 7.2$ is also relatively close to the FRET value of $n = 6$. Finally, the third set of blue diamonds corresponds to a donor placed at $d_D = 6$ nm from the surface of the Au NP. The fit with the dashed blue line yields the values $R_0 = 21$ nm and $n = 8.3$, with an exponent somewhat larger than that for FRET. The inset in Fig. 5(a) shows another fit of the ET efficiency, in the form η', with the same functional form. The fit is now performed by fixing the value of the exponent to the FRET value, i.e., $n = 6$. Thus, there is only one fitting parameter, the characteristic distance R_0. The values obtained from the fit are $R_0 = 28.2$ nm for $d_D = 3$ nm and $R_0 = 18.7$ nm for $d_D = 6$ nm. These are within 10% of the values we obtained from the fit in the main plot, suggesting that the FRET model with increased characteristic distance describes well the ET process over a large range of donor-acceptor distances. When the acceptor is very close to the Au NP, the FRET model no longer strictly applies.

Fig. 5(b) shows similar data, except that now the acceptor is kept at a fixed position, $d_A = 3$ nm and $d_A = 6$ nm, and the distance of the donor to the surface of the Au NP is varied. Fitting the calculations with a power law leads to characteristic distances of $R_0 = 20.1$ nm and $R_0 = 21.6$ nm

with the corresponding values for the exponent $n = 18.6$ and $n = 29.6$. The fitting has, again, been performed in the region where $\eta \approx 50\%$. The extremely large values of the exponent show that, even though the characteristic distances are increased from $R_0 = 9.1$ nm, the FRET model does not apply in this region. The inset shows, however, that one can still use a FRET model, but it is only valid at large separations, where the ET efficiency is extremely low. These separations are larger than the FRET characteristic distance, and, therefore, unlike in the inset of Fig. 5(a), there is no longer any enhancement of the FRET characteristic distance. The inset also shows that the deviation from the FRET model when the donor approaches the surface of the Au NP is now much more dramatic than in Fig. 5(a). For the case of a fixed acceptor, therefore, the interaction between donor and acceptor is enhanced, but the dependence of the ET on this distance does not follow a simple FRET model.

These two panels indicate that, when the donor-Au NP surface separation is constant and small, the donor-Au NP combination acts as a dipole with an enhanced dipole moment, when the acceptor is not very close to the pair. This leads to a FRET, r_{DA}^{-6}, behavior of the ET, with an increased characteristic distance. When the acceptor is brought closer to the pair, it no longer behaves as a single dipole, and the distance dependence becomes more complicated. On the other hand, if the acceptor-Au NP surface separation is constant, the pair does not behave as an enhanced dipole, and a donor brought in its proximity will have a different interaction. This interaction is still considerably increased from the pure donor-acceptor interaction in free-space, as evidenced from the increased characteristic distance — more than doubled — but its distance dependence no longer follows a FRET model and it reverts to the free-space interaction when the donor-pair separation is increased.

Figs. 5(c) and 5(d) extend the data in Fig. 5(a) to a larger range of acceptor distances, up to $d_A = 1$ μm, and to a range of Au NP sizes, from $a = 1$ nm to $a = 1$ μm. This new extended Au NP size range shows an increase in the ET efficiency at larger sizes, $a \approx 50$ nm for $d_D = 3$ nm and $a \approx 100$ nm for $d_D = 6$ nm. This is, most likely, due to the excitation of higher order modes on the Au NP, since it is appreciable when both donor and acceptor are very close to the surface of the Au NP.

3. Angular position dependence of the energy transfer

In Subsection III B 2, the donor and acceptor were placed at opposite sides of the sphere, i.e., at antipodes, and the ET was investigated as a function of their distance to the surface of the sphere alone. We now investigate the influence of the Au NP size on the behavior of the ET efficiency when the angular position of the donor and acceptor around the Au NP is varied. Fig. 6 shows the ET efficiency of a donor-acceptor pair at different distances from the surface of a Au NP as a function of the Au NP size and the angular position of the acceptor around the Au NP. Figs. 6(a) and 6(b) present contour plots of the ET efficiency, η', as a function of Au NP size, a, and acceptor angular position, φ_A, around the Au NP, for a fixed acceptor-Au NP separation, $d_A = 3$ nm and two donor-Au NP separations, $d_D = 3$ nm (Fig. 6(a)) and $d_D = 6$ nm (Fig. 6(b)). Superimposed on the contour plots is a line representing the ET efficiency as a function of the radius at a fixed angular arrangement, $\varphi_A = \pi$. These two panels show that, for large Au NP sizes, $a > 100$ nm, the largest ET efficiency occurs when the donor, Au NP and acceptor lie in a straight line, i.e., when $\varphi_A = \pi$. This is a well-known focusing effect found even for large dielectric spheres. As a function of the Au NP size, the panels show the, by now, familiar increase in the ET efficiency around $a = 100$ nm, again most likely due to higher order modes on the Au NP. There is also a shallower peak at a finite small Au NP size, around $a \approx 6$ nm. This is most likely due to the fact that, for small Au NP sizes, surface scattering effects increase the losses in the gold, but they decrease as the size of the Au NP is increased.

The rest of Figs. 6(c)–6(f), consists of polar plots of the ET efficiency, η, for a fixed donor position at $d_D = 3$ nm, several acceptor positions, $d_A = 2, 3, 6$, and 9 nm, and several Au NP sizes $a = 10$ nm (Fig. 6(c)), $a = 25$ nm (Fig. 6(d)), $a = 50$ nm (Fig. 6(e)), and $a = 75$ nm (Fig. 6(f)). In each panel, the thinner lines are obtained by setting the material of the Au NP to air, effectively calculating the free-space ET efficiency for the same absolute donor-acceptor separation. Beginning with the smallest Au NP size, $a = 10$ nm in Fig. 6(c), the ET efficiency around the Au NP is extremely high, even though its free-space values rapidly decrease (see thinner lines). This is due to the large enhancement of the characteristic distance for a closely spaced ($d_D = 3$ nm) donor-Au NP pair. Increasing the size of the Au NP to $a = 25$ nm as in Fig. 6(d), there is a decrease in the ET efficiency, due to the fact that the actual donor-acceptor distance is now also increased. Around $\varphi_A = \pi$, however, the ET efficiency partially recovers, over quite a broad angular range. This is very similar to the focusing effect observed for much larger spheres, now obtained by very small metal spheres. Finally, the focusing effect is dramatically illustrated in Figs. 6(e) and 6(f), for which the Au NP size is $a = 50$ nm and $a = 75$ nm, respectively. In both panels, the ET efficiency increases at $\varphi_A = \pi$, most dramatically when the acceptor is closest to the Au NP surface. In addition to this large focusing effect, another interesting feature of the ET efficiency in these last two panels is the large number of side lobes at particular angles where the ET efficiency is also increased. We have already seen hints of this behavior in Figs. 6(a), 6(b), and 6(d), but they are much more visible now. These lobes are a result of the excitation of high order modes of Au NP with a large enough size and the interference between these different order modes. If we were to subtract these two effects of focusing and size lobes from the ET efficiency, its angular behavior would be very similar to the free-space case, except corresponding to a smaller overall donor-acceptor separation. This can be seen in the curves corresponding to acceptor position of $d_A = 9$ nm, which show the same "guitar pick" shape as the thinner lines in Fig. 6(c).

4. Spectral overlap dependence of the energy transfer

Finally, we now consider the influence of the Au NP size on the dependence of the ET on the spectral overlap between the donor emission, acceptor absorption, and the LSP peak of the Au NP. To this end we fix the position of the donor and

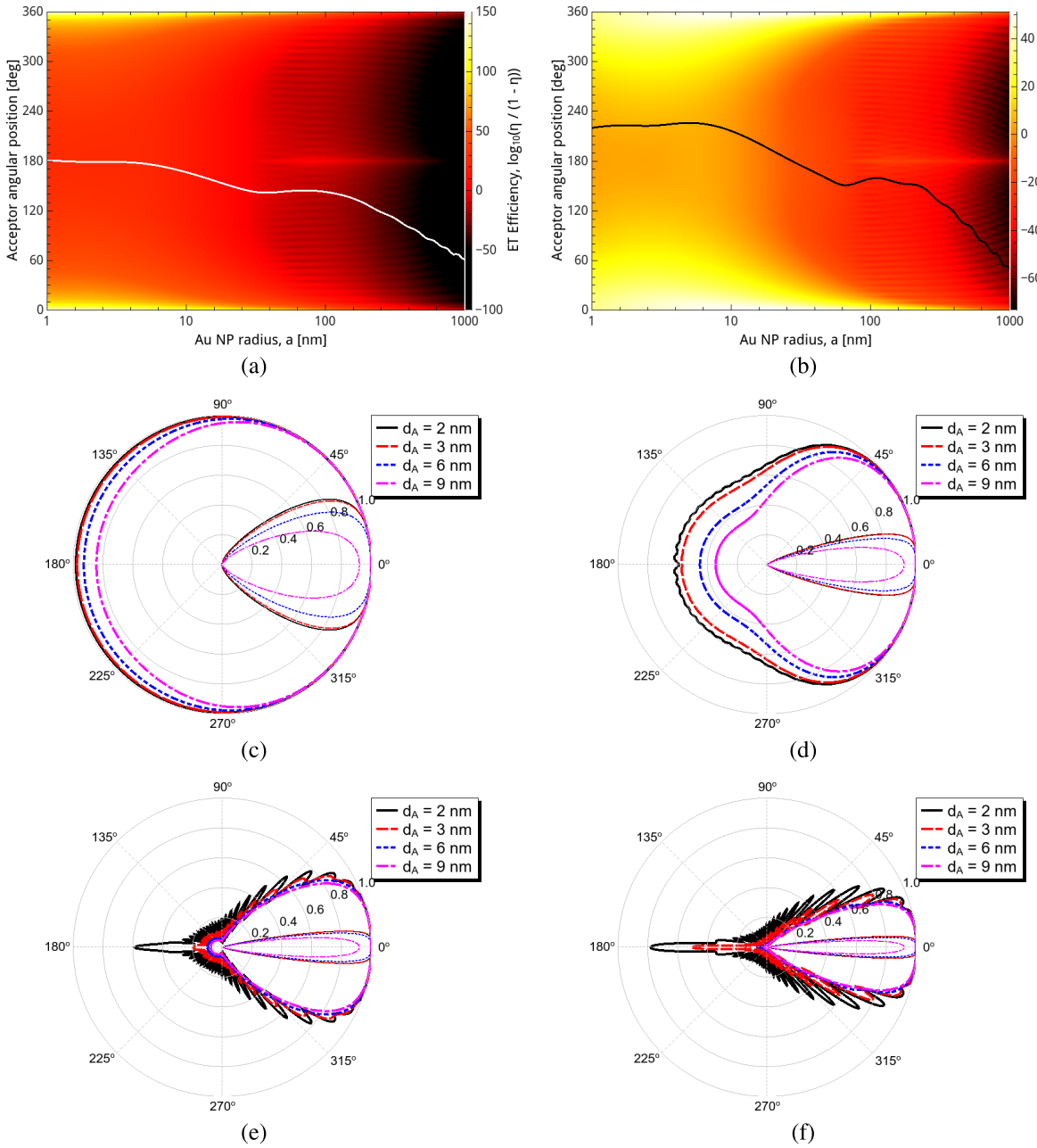

FIG. 6. Contour plots of the ET efficiency, η', as a function of acceptor angular position, φ_A, and Au NP radius, a for fixed acceptor-Au NP surface separation of $d_A = 3$ nm and fixed donor-Au NP surface separation of (a) $d_D = 3$ nm and (b) $d_D = 6$ nm; the lines correspond to a fixed angular position $\varphi_A = \pi$. Polar plot of the ET efficiency, η, as a function of the angular position of the acceptor, φ_A, for a fixed donor-Au NP surface separation, $d_D = 3$ nm and several acceptor-Au NP surface separations (see legends) for different Au NP sizes: (c) $a = 10$ nm, (d) $a = 25$ nm, (e) $a = 50$ nm, and (f) $a = 75$ nm. The donor emission and acceptor absorption peak wavelengths are equal to $\lambda_{em} = \lambda_{abs} = 525$ nm. The orientations of the donor and acceptor dipoles are isotropic. The thin curves correspond to the same donor-acceptor arrangement as the thick curves, but in the absence of the Au NP.

acceptor at several distances from the surface of the Au NP, on opposite sides. We then consider Gaussian distributions with a fixed width of 45 nm for the donor emission spectrum and acceptor absorption spectrum, and we calculate the ET rate as a function of the Au NP size and of the central wavelengths of these distributions (we consider the central wavelength of the donor emission and acceptor absorption spectra to coincide). The results are shown in Fig. 7 for four arrangements of the donor and acceptor around the Au NP, with $d_D = 3$ nm (top row) and $d_D = 6$ nm (bottom row), $d_A = 3$ nm (left column) and $d_A = 6$ nm (right column).

The four panels in Fig. 7 share many similarities with a few notable differences. The main difference consists in the overall values of the ET efficiency, which naturally depend on the donor and acceptor positions relative to the surface of the Au NP. As far as the similarities go, all the panels in the figure show a maximum of the ET efficiency at each Au NP size as a function of wavelength. Indeed, the solid black line in the panels is a guide to the eye to indicate the wavelength corresponding to the maximum ET efficiency as a function of Au NP size. For very small Au NP with a size just above $a = 1$ nm, the wavelength of maximum ET efficiency

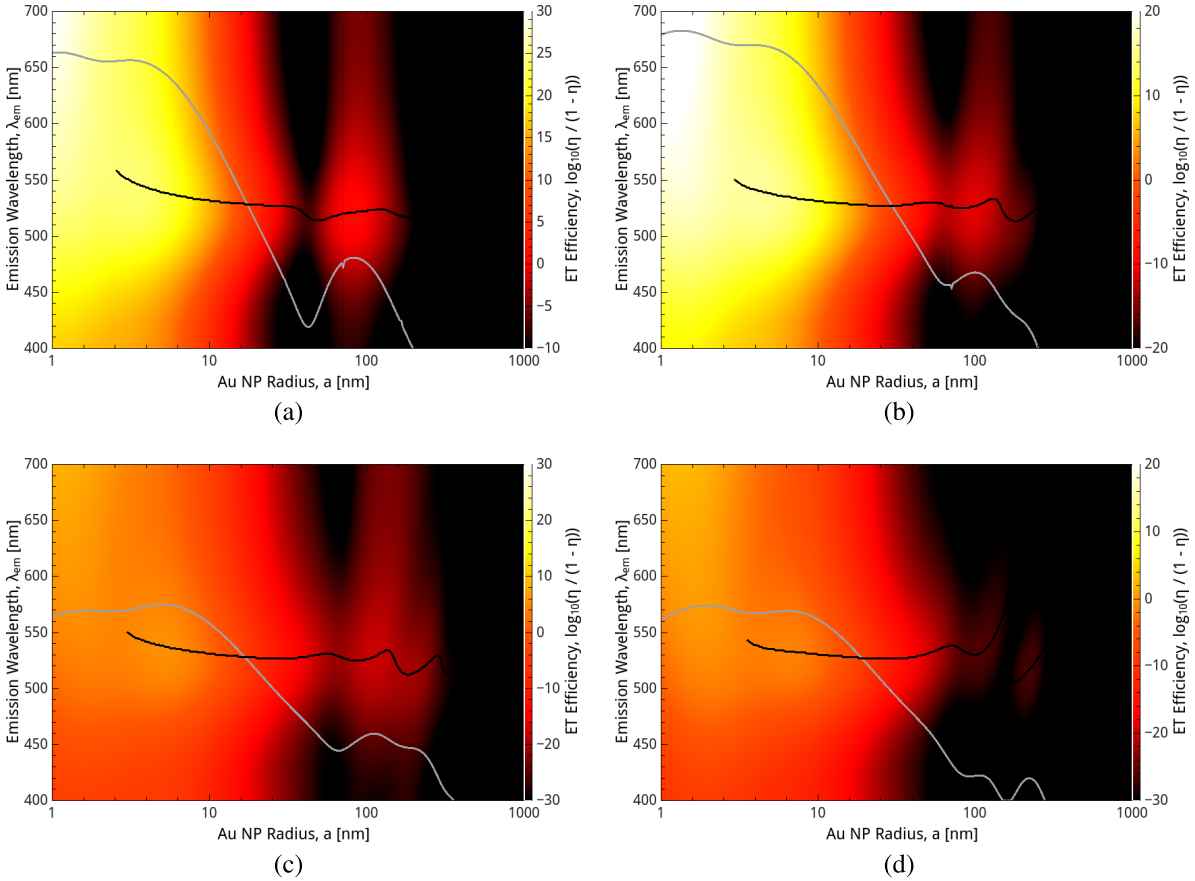

FIG. 7. Contour plots of the ET efficiency, η', as a function of the Au NP size and the central wavelength of the donor emission and acceptor absorption spectra for several positions of the donor and acceptor: (a) and (b) $d_D = 3$ nm, (c) and (d) $d_D = 6$ nm, (a) and (c) $d_A = 3$ nm, and (b) and (d) $d_A = 6$ nm. The light gray lines represent the ET efficiency at a wavelength $\lambda = 525$ nm. The solid black line is a guide to the eye showing the wavelength of the maximum ET efficiency as a function of Au NP size.

is outside our spectral window and we do not show it. Around $a \approx 2.5$ nm, we can define the wavelength of maximum ET efficiency and follow it as the size of the Au NP is increased. There is first a blue-shift of this wavelength from $\lambda \approx 560$ nm to $\lambda \approx 525$ nm, followed by slight oscillations around this value as the size of the Au NP increases more and more. The blue-shift at small Au NP sizes is similar to the blue-shift that the wavelength of the maximum near-field scattering efficiency undergoes as the size of the Au NP is increased. Furthermore, the blue-shift is more pronounced in Fig. 7(a) than in Fig. 7(d), for which both donor and acceptor are further away from the Au NP. The light gray line in all the panels represents the ET efficiency as a function of the Au NP size at a wavelength $\lambda = 525$ nm. The same general structure of the Au NP size dependence can be seen in these panels as we have encountered in Subsections III B 2 and III B 3 large efficiency between $a = 1$ and $a = 10$ nm, followed by an abrupt decrease as the size is increased; a series of much smaller peaks begins around $a = 100$ nm, most likely due to the high order modes of the Au NP.

IV. SUMMARY AND CONCLUSIONS

Though many theoretical calculations and experimental investigations have been performed to study the ET processes in the presence of Au NP, a systematic study is still missing, particularly in relation to the influence of the Au NP size. This is what we have undertaken in this contribution. The formalism used was experimentally verified with the results published elsewhere.[45,74]

We began with the investigation of the ET process between a donor and a Au NP. We employed a Green's tensor formalism to investigate the influence of the Au NP size on the dependence of the non-radiative decay efficiency of a donor close to a Au NP on several parameters, such as the emission wavelength, intrinsic quantum yield of the donor, and the donor-Au NP distance.

We considered the dependence of the non-radiative decay efficiency on the emission wavelength and intrinsic quantum yield of the donor together, since these two parameters are often modified in tandem in experiments. We have found that, for a large range of Au NP sizes, the wavelength dependence of the non-radiative decay efficiency exhibits a peak close to the LSP resonance of the particle. In particular, there is a finite Au NP size for which the non-radiative decay efficiency attains its maximum value. This size depends on the donor-Au NP separation. Very large Au NP are dominated by scattering and higher order modes. The influence of the Au NP size on the quantum yield dependence of the non-radiative decay efficiency follows a similar trend, though now it is the highest quantum yield donor which also has the largest non-radiative decay efficiency for finite size Au NP.

Subsequently, we studied the influence of the Au NP size on the distance dependence of the non-radiative decay efficiency. We found that, for the smallest Au NP, the donor-Au NP interaction follows a FRET model to a good approximation and for a large range of donor-Au NP separations. Both for donor placed very close and very far from the Au NP, the FRET model breaks down. At small separations the donor can couple to the higher-order modes of the Au NP, while at large distances the ET becomes radiative, following a r^{-2} dependence on the donor-Au NP distance. Increasing the size of the NP, the range where the FRET model is valid gradually shrinks and the distance dependence of the non-radiative decay efficiency becomes more complicated.

We have also investigated the influence of the Au NP size on the ET between a donor and acceptor. The ET efficiency is much more sensitive to the donor-Au NP distance, than to the acceptor-Au NP distance. Furthermore, for relatively small Au NP, of a few nanometers in radius, the distance dependence of the ET efficiency for constant donor-Au NP separations suggests that the donor-acceptor interaction mediated by the Au NP is essentially of dipole-dipole type, with a r^{-6} FRET regime, but the strength of the interaction is larger than in free-space. This indicates that the coupling between the donor and the Au NP gives rise to an effective donor with an enhanced dipole moment. The strength of this effective donor dipole moment is very sensitive to the donor-Au NP separation. For larger Au NP sizes, the dipole-dipole approximation breaks down, particularly when the acceptor is in the near-field of the Au NP and can thus interact with the high-order dark modes of the NP. When the acceptor-Au NP separation is fixed, on the other hand, the ET efficiency is substantially different from its free-space value only when both the donor and acceptor are in the near-field region of the Au NP.

The positioning of the donor and acceptor around the sphere can also modify the ET, and we have investigated the influence of the Au NP size on the dependence of the ET efficiency on the angular position of the acceptor. For large Au NP sizes, we have found the well-known focusing effect of spherical particles. This focusing effect also manifests for small Au NP sizes, together with a number of side lobes where the ET efficiency is increased, due to excitation and interference of high order modes on the Au NP.

Finally, we have considered the influence of the Au NP size on the dependence of the ET efficiency between a donor-acceptor pair on the spectral overlap between the donor emission, the acceptor absorption and the Au NP LSP. There are several maxima in the ET efficiency dependence on the Au NP size and the spectral overlap. For the smallest Au NP sizes, the maximum is relatively strongly red-shifted to 570 nm, compared to the LSP peak at 500 nm. Increasing the Au NP size, while still below 10 nm in radius, leads to a blue-shift of the ET efficiency towards the LSP peak. The maximum also occurs for larger Au NP sizes when the donor or acceptor distance to the surface of the NP is larger. This can, again, be attributed to their decoupling from the near-field of the Au NP. The additional maxima in the ET efficiency are weaker and can be found for quite large Au NP sizes, of the order of a few tens to hundreds of nanometers. They are related to higher order modes of the Au NP.

In this contribution, we have undertaken a thorough investigation of the effects of the size of a Au nanosphere on the decay and ET processes of quantum systems placed in its vicinity. The enhanced donor dipole formed by the coupling of the donor quantum system to the Au NP can have interesting applications in improved sensing and as an extended spectroscopic ruler.

ACKNOWLEDGMENTS

This work was supported by the Science Foundation Ireland under Grant No. 10/IN.1/12975.

[1]K. R. Catchpole and A. Polman, Appl. Phys. Lett. **93**, 191113 (2008).
[2]F. J. Beck, A. Polman, and K. R. Catchpole, J. Appl. Phys. **105**, 114310 (2009).
[3]H. Feng Lu, S. Mokkapati, L. Fu, G. Jolley, H. Hoe Tan, and C. Jagadish, Appl. Phys. Lett. **100**, 2010 (2012).
[4]H. A. Atwater and A. Polman, Nat. Mater. **9**, 205 (2010).
[5]J. Henson, E. Dimakis, J. DiMaria, R. Li, S. Minissale, L. Dal Negro, T. D. Moustakas, and R. Paiella, Opt. Express **18**, 21322 (2010).
[6]G. Lozano, D. J. Louwers, S. R. K. Rodríguez, S. Murai, O. T. A. Jansen, M. A. Verschuuren, and J. Gómez Rivas, Light Sci. Appl. **2**, e66 (2013).
[7]L. J. Higgins, V. D. Karanikolas, C. A. Marocico, A. P. Bell, T. C. Sadler, P. J. Parbrook, and A. L. Bradley, Opt. Express **23**, 353 (2015).
[8]N.-Y. Kim, S.-H. Hong, J.-W. Kang, N. Myoung, S.-Y. Yim, S. Jung, K. Lee, C. W. Tu, and S.-J. Park, RSC Adv. **5**, 19624 (2015).
[9]S. Kawata, A. Ono, and P. Verma, Nat. Photonics **2**, 438 (2008).
[10]J. A. Schuller, E. S. Barnard, W. Cai, Y. C. Jun, J. S. White, and M. L. Brongersma, Nat. Mater. **9**, 193 (2010).
[11]C. Sönnichsen, B. M. Reinhard, J. Liphardt, and A. P. Alivisatos, Nat. Biotechnol. **23**, 741 (2005).
[12]K. A. Willets and R. P. Van Duyne, Annu. Rev. Phys. Chem. **58**, 267 (2007).
[13]J. Lee, P. Hernandez, J. Lee, A. O. Govorov, and N. A. Kotov, Nat. Mater. **6**, 291 (2007).
[14]S. Mayilo, M. A. Kloster, M. Wunderlich, A. Lutich, T. A. Klar, A. Nichtl, K. Kürzinger, F. D. Stefani, and J. Feldmann, Nano Lett. **9**, 4558 (2009).
[15]P. K. Jain, X. Huang, I. H. El-Sayed, and M. A. El-Sayed, Acc. Chem. Res. **41**, 1578 (2008).
[16]J. N. Anker, W. P. Hall, O. Lyandres, N. C. Shah, J. Zhao, and R. P. Van Duyne, Nat. Mater. **7**, 442 (2008).
[17]S. Chatterjee, J. B. Lee, N. V. Valappil, D. Luo, and V. M. Menon, Biomed. Opt. Express **2**, 1727 (2011).
[18]R. D. Averitt, D. Sarkar, and N. J. Halas, Phys. Rev. Lett. **78**, 4217 (1997).
[19]S. Berciaud, L. Cognet, P. Tamarat, and B. Lounis, Nano Lett. **5**, 515 (2005).
[20]S. Ancey, Y. Décanini, A. Folacci, and P. Gabrielli, Phys. Rev. B **76**, 195413 (2007).
[21]S. Ancey, Y. Décanini, A. Folacci, and P. Gabrielli, J. Opt. Soc. Am. B **26**, 1176 (2009).
[22]T. J. Davis, D. E. Gómez, and K. C. Vernon, Phys. Rev. B **81**, 045432 (2010).
[23]J. Z. Zhang and C. Noguez, Plasmonics **3**, 127 (2008).
[24]P. Anger, P. Bharadwaj, and L. Novotny, Phys. Rev. Lett. **96**, 113002 (2006).
[25]R. Carminati, J.-J. Greffet, C. Henkel, and J. M. Vigoureux, Opt. Commun. **261**, 368 (2006).
[26]M. Sukharev, N. Freifeld, and A. Nitzan, J. Phys. Chem. C **118**, 10545 (2014).
[27]H. Mertens, A. F. Koenderink, and A. Polman, Phys. Rev. B **76**, 115123 (2007).
[28]J. I. Gersten and A. Nitzan, J. Chem. Phys. **75**, 1139 (1981).
[29]R. Ruppin, J. Chem. Phys. **76**, 1681 (1982).
[30]H. T. Dung, L. Knöll, and D.-G. Welsch, Phys. Rev. A **62**, 053804 (2000).
[31]H. T. Dung, L. Knöll, and D.-G. Welsch, Phys. Rev. A **64**, 013804 (2001).
[32]V. V. Klimov, Opt. Commun. **211**, 183 (2002).
[33]L. A. Blanco and F. J. García de Abajo, J. Quant. Spectrosc. Radiat. Transfer **89**, 37 (2004).
[34]A. O. Govorov, G. W. Bryant, W. Zhang, T. Skeini, J. Lee, N. A. Kotov, J. M. Slocik, and R. R. Naik, Nano Lett. **6**, 984 (2006).
[35]T. Härtling, P. Reichenbach, and L. M. Eng, Opt. Express **15**, 12806 (2007).
[36]A. Moroz, Opt. Commun. **283**, 2277 (2010).
[37]Z. Gueroui and A. Libchaber, Phys. Rev. Lett. **93**, 166108 (2004).
[38]C. S. Yun, A. Javier, T. Jennings, M. Fisher, S. Hira, S. Peterson, B. Hopkins, N. O. Reich, and G. F. Strouse, J. Am. Chem. Soc. **127**, 3115 (2005).

[39]T. L. Jennings, M. P. Singh, and G. F. Strouse, J. Am. Chem. Soc. **128**, 5462 (2006).
[40]T. Pons, I. L. Medintz, K. E. Sapsford, S. Higashiya, A. F. Grimes, D. S. English, and H. Mattoussi, Nano Lett. **7**, 3157 (2007).
[41]M. P. Singh and G. F. Strouse, J. Am. Chem. Soc. **132**, 9383 (2010).
[42]C. J. Breshike, R. A. Riskowski, and G. F. Strouse, J. Phys. Chem. C **117**, 23942 (2013).
[43]G. P. Acuna, M. Bucher, I. H. Stein, C. Steinhauer, A. Kuzyk, P. Holzmeister, R. Schreiber, A. Moroz, F. D. Stefani, T. Liedl, F. C. Simmel, and P. Tinnefeld, ACS Nano **6**, 3189 (2012).
[44]A. Samanta, Y. Zhou, S. Zou, H. Yan, and Y. Liu, Nano Lett. **14**, 5052 (2014).
[45]X. Zhang, C. A. Marocico, M. Lunz, V. A. Gerard, Y. K. Gun'ko, V. Lesnyak, N. Gaponik, A. S. Susha, A. L. Rogach, and A. L. Bradley, ACS Nano **6**, 9283 (2012).
[46]P. Reineck, D. Gómez, S. H. Ng, M. Karg, T. Bell, P. Mulvaney, and U. Bach, ACS Nano **7**, 6636 (2013).
[47]R. Chhabra, J. Sharma, H. Wang, S. Zou, S. Lin, H. Yan, S. Lindsay, and Y. Liu, Nanotechnology **20**, 485201 (2009).
[48]M. Li, S. K. Cushing, Q. Wang, X. Shi, L. A. Hornak, Z. Hong, and N. Wu, J. Phys. Chem. Lett. **2**, 2125 (2011).
[49]E. Dulkeith, A. Morteani, T. Niedereichholz, T. Klar, J. Feldmann, S. Levi, F. van Veggel, D. Reinhoudt, M. Möller, and D. Gittins, Phys. Rev. Lett. **89**, 203002 (2002).
[50]R. M. Clegg, Curr. Opin. Biotechnol. **6**, 103 (1995).
[51]J. Lai, B. P. Shah, E. Garfunkel, and K.-B. Lee, ACS Nano **7**, 2741 (2013).
[52]J. Chen, N. K. Poddar, L. J. Tauzin, D. Cooper, A. B. Kolomeisky, and C. F. Landes, J. Phys. Chem. B **118**, 12130 (2014).
[53]E. D. Holmstrom and D. J. Nesbitt, J. Phys. Chem. B **118**, 3853 (2014).
[54]M. Achermann, M. A. Petruska, D. D. Koleske, M. H. Crawford, and V. I. Klimov, Nano Lett. **6**, 1396 (2006).
[55]H. V. Demir, S. Nizamoglu, T. Erdem, E. Mutlugun, N. Gaponik, and A. Eychmüller, Nano Today **6**, 632 (2011).
[56]S. Chanyawadee, R. T. Harley, D. Taylor, M. Henini, A. S. Susha, A. L. Rogach, and P. G. Lagoudakis, Appl. Phys. Lett. **94**, 134 (2009).
[57]M. Achermann, M. A. Petruska, S. Kos, D. L. Smith, D. D. Koleske, and V. V. Klimov, Nature **429**, 642 (2004).
[58]S. Nizamoglu, E. Mutlugun, O. Akyuz, N. Kosku Perkgoz, H. Volkan Demir, L. Liebscher, S. Sapra, N. Gaponik, and A. Eychmüller, New J. Phys. **10**, 023026 (2008).
[59]S. Chanyawadee, P. G. Lagoudakis, R. T. Harley, M. D. B. Charlton, D. V. Talapin, H. W. Huang, and C. H. Lin, Adv. Mater. **22**, 602 (2010).
[60]S. Nizamoglu, P. Ludwig Hernández-Martínez, E. Mutlugun, D. Ugur Karatay, and H. Volkan Demir, Appl. Phys. Lett. **100**, 241109 (2012).
[61]R. M. Clegg, in *Fluorescence Imaging Spectroscopy and Microscopy*, edited by X. F. Wang and B. Herman (John Wiley & Sons, Inc., New York, NY, USA, 1996), Vol. 137, p. 179.
[62]B. W. Van Der Meer, G. Coker, and S. Y. Chen, *Resonance Energy Transfer: Theory and Data* (Wiley, New York, NY, USA, 1994), p. 177.
[63]I. L. Medintz, A. R. Clapp, H. Mattoussi, E. R. Goldman, B. Fisher, and J. M. Mauro, Nat. Mater. **2**, 630 (2003).
[64]W. R. Algar, H. Kim, I. L. Medintz, and N. Hildebrandt, Coord. Chem. Rev. **263-264**, 65 (2014).
[65]L. Stryer and R. P. Haugland, Proc. Natl. Acad. Sci. U. S. A. **58**, 719 (1967).
[66]T. Förster, Ann. Phys. **437**, 55 (1948).
[67]J. Zhang, Y. Fu, and J. R. Lakowicz, J. Phys. Chem. C **111**, 50 (2007).
[68]J. Zhang, Y. Fu, M. H. Chowdhury, and J. R. Lakowicz, J. Phys. Chem. C **111**, 11784 (2007).
[69]V. Faessler, C. Hrelescu, A. Lutich, L. Osinkina, S. Mayilo, F. Jäckel, and J. Feldmann, Chem. Phys. Lett. **508**, 67 (2011).
[70]M. Lessard-Viger, M. Rioux, L. Rainville, and D. Boudreau, Nano Lett. **9**, 3066 (2009).
[71]M. Lunz, V. A. Gerard, Y. K. Gun'ko, V. Lesnyak, N. Gaponik, A. S. Susha, A. L. Rogach, and A. L. Bradley, Nano Lett. **11**, 3341 (2011).
[72]M. Lunz, X. Zhang, V. A. Gerard, Y. K. Gun'ko, V. Lesnyak, N. Gaponik, A. S. Susha, A. L. Rogach, and A. L. Bradley, J. Phys. Chem. C **116**, 26529 (2012).
[73]T. Ozel, P. L. Hernandez-Martinez, E. Mutlugun, O. Akin, S. Nizamoglu, I. O. Ozel, Q. Zhang, Q. Xiong, and H. V. Demir, Nano Lett. **13**, 3065 (2013).
[74]X. Zhang, C. A. Marocico, M. Lunz, V. A. Gerard, Y. K. Gun'ko, V. Lesnyak, N. Gaponik, A. S. Susha, A. L. Rogach, and A. L. Bradley, ACS Nano **8**, 1273 (2014).
[75]R. G. West and S. M. Sadeghi, J. Phys. Chem. C **116**, 20496 (2012).
[76]L. Zhao, T. Ming, L. Shao, H. Chen, and J. Wang, J. Phys. Chem. C **116**, 8287 (2012).
[77]P. Ghenuche, J. De Torres, S. B. Moparthi, V. Grigoriev, and J. Wenger, Nano Lett. **14**, 4707 (2014).
[78]J. I. Gersten and A. Nitzan, Chem. Phys. Lett. **104**, 31 (1984).
[79]X. M. Hua, J. I. Gersten, and A. Nitzan, J. Chem. Phys. **83**, 3650 (1985).
[80]A. O. Govorov, J. Lee, and N. Kotov, Phys. Rev. B **76**, 125308 (2007).
[81]H. Xie, H. Chung, P. Leung, and D. Tsai, Phys. Rev. B **80**, 155448 (2009).
[82]M. K. Schmidt and S. Mackowski, Open Phys. **9**, 562 (2011).
[83]J. A. Gonzaga-Galeana and J. R. Zurita-Sánchez, J. Chem. Phys. **139**, 244302 (2013).
[84]H. T. Dung, L. Knöll, and D.-G. Welsch, Phys. Rev. A **65**, 043813 (2002).
[85]C. A. Marocico and J. Knoester, Phys. Rev. A **79**, 053816 (2009).
[86]C. A. Marocico and J. Knoester, Phys. Rev. A **84**, 053824 (2011).
[87]L. Novotny and B. Hecht, *Principles of Nano-Optics*, 2nd ed. (Cambridge University Press, Cambridge, UK, 2012).
[88]G. Decher, Science **277**, 1232 (1997).
[89]R.-L. Chern, X.-X. Liu, and C.-C. Chang, Phys. Rev. E **76**, 016609 (2007).
[90]P. K. Wolber and B. S. Hudson, Biophys. J. **28**, 197 (1979).